Impact of longitudinal fields on second harmonic generation in lithium niobate nanopillars

Mohammad Amin Baghban and Katia Gallo

Citation: APL Photonics **1**, 061302 (2016); doi: 10.1063/1.4953670
View online: http://dx.doi.org/10.1063/1.4953670
View Table of Contents: http://aip.scitation.org/toc/app/1/6
Published by the American Institute of Physics

Articles you may be interested in

Invited Article: Broadband highly efficient dielectric metadevices for polarization control
APL Photonics **1**, 030801030801 (2016); 10.1063/1.4949007

Anti-reflective surfaces: Cascading nano/microstructuring
APL Photonics **1**, 076104076104 (2016); 10.1063/1.4964851

Invited Article: Precision nanoimplantation of nitrogen vacancy centers into diamond photonic crystal cavities and waveguides
APL Photonics **1**, 020801020801 (2016); 10.1063/1.4948746

Single-mode optical waveguides on native high-refractive-index substrates
APL Photonics **1**, 071302071302 (2016); 10.1063/1.4955065

Resolving the mystery of milliwatt-threshold opto-mechanical self-oscillation in dual-nanoweb fiber
APL Photonics **1**, 056101056101 (2016); 10.1063/1.4953373

Gold-reinforced silver nanoprisms on optical fiber tapers—A new base for high precision sensing
APL Photonics **1**, 066102066102 (2016); 10.1063/1.4953671

APL PHOTONICS **1**, 061302 (2016)

Impact of longitudinal fields on second harmonic generation in lithium niobate nanopillars

Mohammad Amin Baghban and Katia Gallo[a]
Department of Applied Physics, School of Engineering Sciences, KTH–Royal Institute of Technology, Stockholm SE-106 91, Sweden

(Received 10 March 2016; accepted 30 May 2016; published online 14 July 2016)

An optimized focused ion beam process is used to fabricate micrometer-long $LiNbO_3$ nanopillars with diameters varying between 150 and 325 nm. Polarimetric mappings of second harmonic generation from a wavelength of 850 nm demonstrate the ability to modify the polarization features of the nonlinear response through a fine adjustment of the pillar size. The effect is ascribed to the non-negligible contribution of the longitudinal fields associated with sub-wavelength light confinement in the $LiNbO_3$ nanopillars. The results also highlight the importance of a fine control over the nanopillar size in order to effectively engineer their nonlinear response. © *2016 Author(s). All article content, except where otherwise noted, is licensed under a Creative Commons Attribution (CC BY) license (http://creativecommons.org/licenses/by/4.0/).* [http://dx.doi.org/10.1063/1.4953670]

The longitudinal fields arising in tightly confined optical beams give rise to unique polarization properties amenable to, e.g., particle acceleration[1] and optical tweezing,[2] and have also important implications on, e.g., optical chirality[3] and nonlinear optical processes.[4–6] While large longitudinal fields are typically created in free space with radially or azimuthally polarized beams,[4] recent trends in the miniaturization of photonic devices make nowadays integrated approaches also viable.[4,5,7–9]

Lithium niobate ($LiNbO_3$) is a cornerstone material for second-order nonlinear optics.[10,11] Sub-wavelength structures in $LiNbO_3$ are currently attracting considerable attention in light of the nonlinear efficiency enhancements afforded by their tight field confinement.[12–14] They can also be expected to sustain non-negligible longitudinal field components, leading to qualitatively different features in the nonlinear response, which have nevertheless not yet been addressed in such investigations.

In this letter, we study the polarization features of second harmonic generation (SHG) from $LiNbO_3$ cylindrical nanopillars (NPs) with diameters ranging from 150 nm to 325 nm and demonstrate substantial modifications to their SHG polar emission, achieved through a fine adjustment of their size. Experiments and simulations for high-confinement guided-wave SHG in congruent z-cut $LiNbO_3$ NPs, from a fundamental wavelength of 850 nm, provide evidence for a marked deviation of the NP response from the bulk material, maximized for a NP diameter of 275 nm. The effect stems from a non-negligible contribution to SHG arising from the longitudinal components of the optical modes confined in the NPs and points out to new possibilities afforded by advanced $LiNbO_3$ nano-structuring technologies in order to tailor not only the efficiency but also the radiation patterns of nanoscopic emitters on this important nonlinear photonic platform.

The nanopillars were fabricated on commercial, 500 μm–thick, congruent z-cut $LiNbO_3$ substrates (CasTech, Inc.) by an optimized Focused Ion Beam (FIB) milling process, yielding NPs with heights of ~1 μm, circular cross sections and nearly vertical sidewalls (~85°). The average value (due to the 85° slope) of the NP diameters was varied controllably between 150 and 325 nm in steps of 25 nm. To limit drifting of the ion beam, a 40 nm-thick layer of chromium was deposited on

[a]Author to whom correspondence should be addressed. Electronic mail: gallo@kth.se.

 © Author(s) 2016.

the $LiNbO_3$ surface prior to the FIB milling. The ion beam milling current (30 pA) and its dwell time (2 μs) were adjusted while raster-scanning the ion beam, in order to obtain the best quality NP sidewalls. Each NP was embedded into a much larger (2.8 μm-wide, 1 μm-deep) circular trench to minimize spurious contributions of the bulk material in the SHG measurements. Figure 1(a) shows one of the fabricated structures, while Figs. 1(b) and 1(c) illustrate the spatial distributions of the transverse and longitudinal optical fields [$E_t(x, y)$ and $E_z(x, y)$] at the fundamental frequency (FF) and at its second harmonic (SH), computed with a finite element solver (COMSOL) for the case of perfectly vertical NPs, in the crystal reference frame (x, y, z). At the FF (850 nm), NPs with diameters smaller than 320 nm support only the lowest-order, $HE_{11}{}^{(x)}$ and $HE_{11}{}^{(y)}$ (orthogonally polarized and index-degenerate) modes, while being highly multimode at SH (425 nm) [$HE_{11}{}^{(x)}$, $HE_{11}{}^{(y)}$, TE_{01}, $HE_{21}{}^{(x)}$, $HE_{21}{}^{(y)}$, TM_{01}, ...].

The SHG experiments were conducted in the transmission configuration of Fig. 1(d). The FF pump was a pulsed Ti:sapphire laser (100 fs pulse width, 82 MHz repetition rate, 850 nm central wavelength). The incident FF beam was linearly polarized in the $x - y$ plane of the crystal and its polarization direction was adjusted by rotation of a half-wave plate with an angular resolution of 5°. The FF free space pump was coupled into the NPs by an infinity-corrected 50× microscope objective. The sample position was adjusted with a precision three-dimensional stage, aligning the beam propagation direction to the z-axis of the crystal. Measurements in the bulk (reference case) and on individual NPs were all performed under the same excitation conditions, with a weakly focused FF pump (2 μm spot-size) and at room temperature. The output SH signals were collected in transmission-mode by another 50× objective, followed by a high-pass filter (to remove the FF) and by a polarizer which selected the polarization component of the SH, finally detected by a monochromator coupled to a single photon detector.

Figure 2 (Multimedia view) shows the SHG polar plots for experiments performed on z-cut NPs, with a fixed polarization of the SH output (along x) and a varying polarization of the FF input (angle θ in the $x - y$ plane of the crystal).

In order to compare the SHG powers across the different measurements, for each of the plots in Figs. 2(a)-2(h) (Multimedia view) we provide also the value of the power scaling factor (N) with respect to the measurement on bulk $LiNbO_3$ [Fig. 2(i)]. The maximum SH powers generated by the NPs are comparable or even higher than in the bulk, even if the large size of the FF pump (chosen to

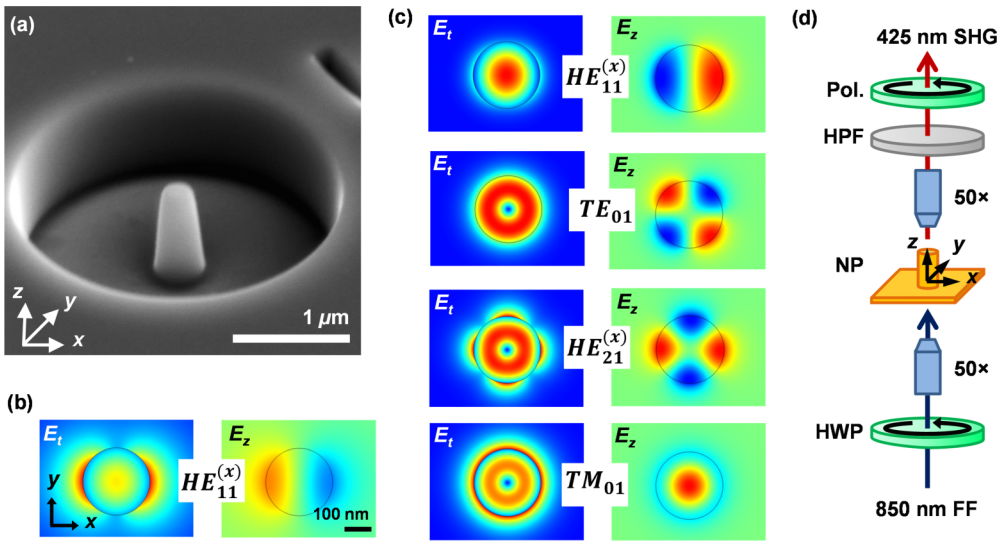

FIG. 1. (a) Tilted (52°) scanning electron microscopy (SEM) image of a 325 nm NP in z-cut $LiNbO_3$. Examples of calculated transverse (x, y) distributions of the transverse (E_t) and longitudinal (E_z) field components supported by a 275 nm NP; (b) $HE_{11}{}^{(x)}$ mode at $\lambda_{FF} = 850$ nm; (c) $HE_{11}{}^{(x)}$, TE_{01}, $HE_{21}{}^{(x)}$, and TM_{01} modes at $\lambda_{SH} = 425$ nm. (d) Sketch of the experimental configuration used to measure SHG in the NPs: HWP: half-wave plate, 50×: infinity corrected 50× objective, HPF: high pass filter, Pol.: polarizer. (x, y, z) are the $LiNbO_3$ crystallographic axes.

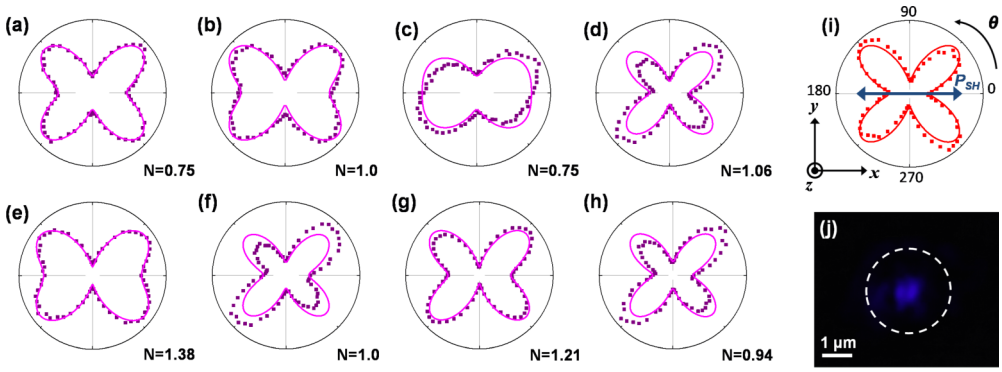

FIG. 2. Polar plots for x-polarized SHG in z-cut $LiNbO_3$, measured as a function of the input FF polarization (θ) in NPs of different diameters: (a) 325 ± 42 nm, (b) 300 ± 40 nm, (c) 275 ± 40 nm, (d) 250 ± 31 nm, (e) 225 ± 36 nm, (f) 200 ± 43 nm, (g) 175 ± 27 nm, (h) 150 ± 26 nm. The ± terms indicate the diameter variation from top to bottom of each NP (due to their sidewall slope) and in (i) bulk z-cut substrate. Markers: experimental raw data. Solid lines: numerical fits based on Eq. (2). The scaling factor N represents the maximum power of each polar plot with respect to that of bulk $LiNbO_3$. (j) Image of the SH generated inside a 300 nm NP. The dashed circle highlights the trench border. (Multimedia view) [URL: http://dx.doi.org/10.1063/1.4953670.1]

minimize longitudinal field contributions in the bulk measurements) is not optimal for efficient light coupling in them. As seen from image in Fig. 2(j), SHG in the NP provides an intense blue source, much more tightly localized than the infrared FF pump.

A first qualitative picture of SHG can be obtained under the simplifying assumptions of no-pump-depletion and perfect phase-matching, considering the relationship induced by the $LiNbO_3$ tensorial nonlinearity between the SH polarization [$P_x^{(SH)}$, $P_y^{(SH)}$, $P_z^{(SH)}$] and the FF electric field [$E_x^{(FF)}$, $E_y^{(FF)}$, $E_z^{(FF)}$] vectors.[15] Specifically, for Fig. 2, the relevant polarization term is of the form

$$P_x^{(SH)} = -2\varepsilon_0 d_{22} E_x^{(FF)} E_y^{(FF)} + 2\varepsilon_0 d_{31} E_x^{(FF)} E_z^{(FF)}, \quad (1)$$

where d_{31} = 4.8 pm/V and d_{22} = 2.2 pm/V are $LiNbO_3$ nonlinear coefficients,[16] and the dependence of the transverse field components is adjusted by the polarization angle θ as follows: $E_x^{(FF)} = E_0 \cos\theta$ and $E_y^{(FF)} = E_0 \sin\theta$, where E_0 is the total FF field amplitude.

The first term in Eq. (1) is *purely transverse* and gives rise to a contribution to the SHG power ($P_a \propto \cos^2\theta \sin^2\theta$) corresponding to the polar plot of Fig. 3(a), with maxima at θ = +45°. This polar response matches well with the one of bulk measurements [Fig. 2(i) (Multimedia view)], indicating a negligible contribution from the longitudinal field $E_z^{(FF)}$ in this case, which is consistent with the relatively weak focusing of the FF pump (2 μm spot-size) used in the experiments.

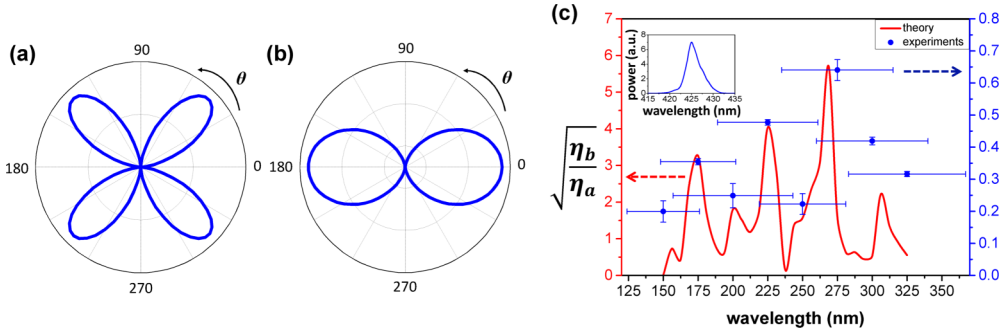

FIG. 3. Polar plots of x-polarized SH intensity, in a z-cut NP, as a function of the input FF polarization angle (θ), calculated for the two limit cases of: (a) *purely transverse* and (b) *longitudinal-transverse* SHG coupling. (c) Evolution of $\sqrt{\eta_b/\eta_a}$ as a function of the (median) NP diameter, quantifying the strength of SHG driven by FF longitudinal field. Red solid curve: theoretical predictions. Blue circles: experimental data. Inset: spectrum of the SH signal.

The second term in Eq. (1) involves a coupling of the *transverse* and *longitudinal* FF fields. Considering in a first instance the latter as a constant, independent of θ and proportional to E_0, results in a contribution to the SHG power ($P_b \propto \cos^2\theta$) corresponding to the polar plot of Fig. 3(b), elongated along the x-axis. The presence of such additional SHG component is apparent in the SHG measurements from the NPs, being maximized for Fig. 2(c). The polar plot deformation indicates a non-negligible role of the longitudinal mode component, associated with the strong field confinement in the NP, as opposed to the bulk, consistent with the indications of numerical simulations [e.g., Fig. 1(b), where $E_z \sim 70\%\ E_t$].

The above insights were combined with a more rigorous analysis of SHG in a tight field confinement regime, accounting for the full vectorial nature of the electric fields as determined from Maxwell's equations. This involved modelling the NPs as high confinement waveguides,[9] computing first their modal fields and effective indices, and then the SHG coupling strengths and wavevector mismatches for all possible combinations of FF and SH modes and polarization components in the NP. After identifying the dominant modal contributions to SHG (Table I), we used a guided-wave coupled-mode approach, accounting also for the E_z terms,[17,18] to determine the SH output after a propagation length of $L = 1\ \mu$m. Restricting the analysis to NP waveguides supporting only HE_{11} modes at the FF, and using the undepleted-pump approximation, ultimately yielded the following functional dependence of the x-polarized SHG power on the FF polarization angle θ,

$$P_{SHG} = \eta_a \sin^2\theta \cos^2\theta + \eta_b \cos^4\theta, \tag{2}$$

where η_a and η_b summarize the main contributions to SHG, which arise from the interactions listed in Table I and labelled with the index $m = 1, \ldots, 5$. Specifically $\eta_a = \eta_1 + \eta_2 + \eta_3$ and $\eta_b = \eta_4 + \eta_5$, with $\eta_m = {\kappa_m}^2\ \mathrm{sinc}^2(\Delta\beta_m L/2)$, where κ_m and $\Delta\beta_m$ are the SHG coupling coefficients and wave-vector mismatches (computed numerically for each NP) for each of the processes in Table I.

Based on Eq. (2), quantitative estimates of the coefficients η_a and η_b could be extracted from the experiments via numerical fits on the data of Fig. 2 (solid lines). From such fits, one could obtain a figure of merit: $FOM_{(\mathrm{EXP})} = \sqrt{(\eta_b/\eta_a)}\big|_{(EXP)}$, quantifying the deviation of the polar response from the bulk (where $FOM \to 0$). These experimental values were then compared with the estimates for the $FOM_{(\mathrm{TH})} = \sqrt{(\eta_b/\eta_a)}\big|_{(TH)}$ computed as a function of the NP size, with the SHG coupled-mode approach outlined before.

Fig. 3(c) shows the evolution of the experimental (blue markers) and theoretical (solid line) figures of merit as a function of the NP (median) width in the 150-325 nm range, which confirms the first insights provided by the qualitative comparison of the data of Fig. 2 (Multimedia view) with Figs. 3(a) and 3(b). The contribution of the longitudinal components in the experiments is maximized for a NP diameter of 275 nm [Fig. 2(d)], which compares well with the simulations (269 nm). Theory and experiments in Fig. 3(c) follow a similar trend, exhibiting additional local maxima around 175 and 225 nm. The agreement is quite good, even if the NPs used in the experiments deviate from the ideal structures used in the simulations, due to the slope of their sidewalls (see Fig. 1(a)). This yields a diameter variation (across the NP length) around the median values reported in Fig. 3(c) and should induce a smearing of the experimental *FOM*. The horizontal error bars in Fig. 3(c) indicate the extent of the (linear) variation of the NP diameter around the median values.

TABLE I. List of the five main interactions (in terms of guided modes and field components) contributing to $x-$ polarized SHG in z-cut NPs with diameters below 320 nm (only HE_{11} modes at FF).

Index m	FF modes	SH mode	Field components
1	${HE_{11}}^{(x)} + {HE_{11}}^{(y)}$	HE_{11}	$xy \to x$
2	${HE_{11}}^{(x)} + {HE_{11}}^{(y)}$	HE_{12}	$xx \to x$
3	${HE_{11}}^{(x)} + {HE_{11}}^{(y)}$	TE_{01}	$zy \to y$
4	${HE_{11}}^{(x)} + {HE_{11}}^{(x)}$	HE_{21}	$xz \to x$
5	${HE_{11}}^{(x)} + {HE_{11}}^{(x)}$	TM_{01}	$xz \to x$

Such a variation is also responsible for a decrease in efficiency with respect to the theoretical predictions for perfectly vertical NPs. This effect, together with a non-perfect removal of the bulk SHG background in the experiments, is at the origin of the difference between the theoretical and experimental FOM values, i.e., the different scales on the left and right axes, respectively, of Fig. 3(c).

Furthermore, the non-monotonic evolution of the *FOM* as a function of the NP diameter, seen in both theory and experiments, highlights the importance of a fine control over their (median) diameter (~25 nm) in order to optimize the SHG polar response. The effect stems from a non-trivial interplay among the parameters (κ_m and $\Delta\beta_m$) determining the strength of competing SHG processes in the NP, which are critically affected by the NP size.

In conclusion, micrometer-long z-cut $LiNbO_3$ NPs with diameters ranging from 150 nm to 325 nm and nearly vertical sidewalls were fabricated using an optimized focused-ion-beam milling process. With them we demonstrated the possibility to modify and control the polarization properties of SHG emission in $LiNbO_3$, via the contribution of the longitudinal fields associated with subwavelength confinement. SHG experiments with a pump at a wavelength of 850 nm, in combination with theoretical analyses based on guided-wave coupled-mode theory in a high confinement regime, indicated that the effect is maximized for a diameter of 275 nm. They also made apparent the importance of an accurate control over the NP size (<25 nm) in order to effectively engineer the SHG polar emission properties.

The results provide experimental evidence for new degrees of freedom in engineering nanoscopic nonlinear devices in $LiNbO_3$ affordable via the large longitudinal fields sustained by tight guided-wave confinement. They pave the way for the implementation of ultra-compact frequency converters with tailored emission, potentially enabling novel miniaturized photonic devices which can leverage the high intrinsic optical nonlinearity of $LiNbO_3$ for such applications as single-molecule spectroscopy, quantum optics, sensing, and all-optical beam manipulation. The fabrication process is also amenable to the production of dense NP arrays, which can grant further efficiency enhancements and engineering degrees of freedom in shaping the SHG response, currently under investigation.

We gratefully acknowledge the kind assistance of Dr. Marcin Swillo in the experiments and support to this research from the ADOPT Linnaeus Centre and the Swedish Research Council (Projects No. 622-2010-526 and 621-2014-5407).

[1] M. O. Scully and M. S. Zubairy, Phys. Rev. A **44**(4), 2656–2663 (1991).
[2] Y. Zhao, Q. Zhan, Y. Zhang, and Y.-P. Li, Opt. Lett. **30**(8), 848–850 (2005).
[3] J. Petersen, J. Volz, and A. Rauschenbeutel, Science **346**(6205), 67–71 (2014).
[4] G. Bautista, J. Mäkitalo, Y. Chen, V. Dhaka, M. Grasso, L. Karvonen, H. Jiang, M. J. Huttunen, T. Huhtio, H. Lipsanen, and M. Kauranen, Nano Lett. **15**(3), 1564–1569 (2015).
[5] R. Sanatinia, M. Swillo, and S. Anand, Nano Lett. **12**(2), 820–826 (2012).
[6] P. R. Wiecha, A. Arbouet, H. Kallel, P. Periwal, T. Baron, and V. Paillard, Phys. Rev. B **91**(12), 121416 (2015).
[7] J. B. Driscoll, X. Liu, S. Yasseri, I. Hsieh, J. I. Dadap, and R. M. Osgood, Opt. Express **17**(4), 2797–2804 (2009).
[8] M. A. Foster, A. C. Turner, M. Lipson, and A. L. Gaeta, Opt. Express **16**(2), 1300–1320 (2008).
[9] R. Sanatinia, S. Anand, and M. Swillo, Nano Lett. **14**(9), 5376–5381 (2014).
[10] L. E. Myers, R. C. Eckardt, M. M. Fejer, R. L. Byer, W. R. Bosenberg, and J. W. Pierce, J. Opt. Soc. Am. B **12**(11), 2102–2116 (1995).
[11] S. Liu, K. J. Lee, F. Parmigiani, J. Kakande, K. Gallo, P. Petropoulos, and D. J. Richardson, Opt. Express **19**(12), 11705–11715 (2011).
[12] A. Sergeyev, R. Geiss, A. S. Solntsev, A. Steinbrück, F. Schrempel, E.-B. Kley, T. Pertsch, and R. Grange, Opt. Express **21**(16), 19012–19021 (2013).
[13] F. Dutto, M. Heiss, A. Lovera, O. López-Sánchez, A. Fontcuberta i Morral, and A. Radenovic, Nano Lett. **13**(12), 6048–6054 (2013).
[14] D. Lehr, J. Reinhold, I. Thiele, H. Hartung, K. Dietrich, C. Menzel, T. Pertsch, E.-B. Kley, and A. Tünnermann, Nano Lett. **15**(2), 1025–1030 (2015).
[15] R. Boyd, *Nonlinear Optics* (Academic Press, Burlington, 2008).
[16] R. S. Weis and T. K. Gaylord, Appl. Phys. A **37**(4), 191–203 (1985).
[17] H. Nishihara, M. Haruna, and T. Suhara, *Optical Integrated Circuits* (McGraw-Hill, 1989).
[18] S. V. Afshar and T. M. Monro, Opt. Express **17**(4), 2298–2318 (2009).